Stability and Reactivity of Aromatic Radical Anions in Solution with Relevance to Birch Reduction

Tatiana Nemirovich*,[1] Brandon Young*,[2] Krystof Brezina*,[1] Philip E. Mason,[1] Robert Seidel,[3] Dominik Stemer,[4] Bernd Winter,[4] Pavel Jungwirth,[1] Stephen E. Bradforth,[2, a)] and H. Christian Schewe[1, b)]

[1)] *Institute of Organic Chemistry and Biochemistry of the Czech Academy of Sciences, Flemingovo nám. 2, 166 10 Prague 6, Czech Republic*

[2)] *Department of Chemistry, University of Southern California, Los Angeles, California 90089, United States*

[3)] *BESSY II*

[4)] *FHI berlin*

(Dated: 2 October 2023)

We investigate the electronic structure of aromatic radical anions in the solution phase employing a combination of liquid-jet (LJ) photoelectron (PE) spectroscopy measurements and quantum chemical calculations. By employing recently developed protocols we accurately determine the vertical detachment energies (VDEs) of valence electrons of both the solvent molecules and the solutes. In particular, we first characterize the pure solvent of tetrahydrofuran (THF) by LJ-PE measurements in conjunction with ab-initio molecular dynamics (AIMD) simulations and G_0W_0 calculations. Next, we determine using the same methods the electronic structure of neutral naphthalene (Np) and benzophenone (Bp) as well as their radical anion counterparts Np^- and Bp^- in THF. Wherever feasible, we performed orbital assignments of the measured PE features of the aromatic radical anions, with comparisons to UV-vis absorption spectra of the corresponding neutral molecules being instrumental in rationalizing the assignments. Analysis of the electronic structure differences between the neutral species and their anionic counterparts provides understanding of the primarily electrostatic stabilization of the radical anions in solution. Finally, we obtain a very good agreement of the reductive potentials extracted from the present LJ-PES measurements of Np^- and Bp^- in THF with previous electrochemical data from cyclic voltammetry measurements. In this context, we discuss how the choice of solvent holds significant implications for optimizing conditions for the Birch reduction process, wherein aromatic radical anions play crucial roles as reactive intermediates.

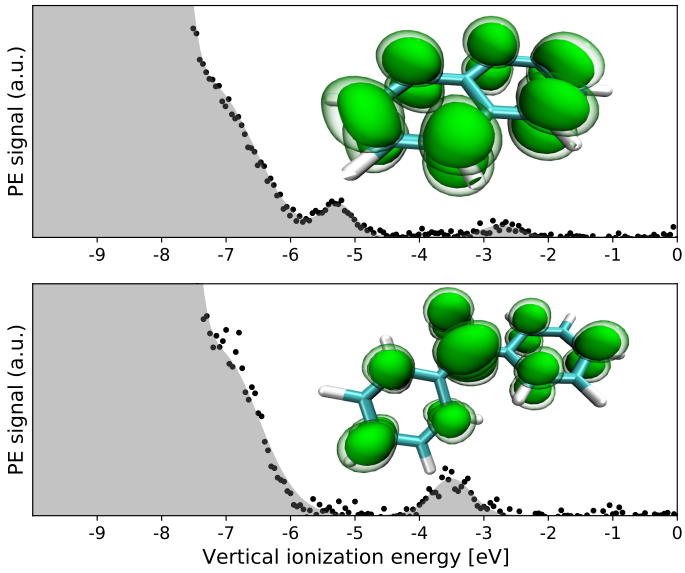

1. INTRODUCTION

Radical anions of aromatic hydrocarbons represent key reaction intermediates in areas spanning organic, inorganic, and organometallic chemistry.[1] Among the well-known examples is the Birch reduction,[2] wherein aromaticity in arenes is disrupted, leading to the formation of non-conjugated cyclohexadienes. These processes are exploited on synthetic and industrial scales to produce steroids and other drugs.[3] Radical anions of aromatic hydrocarbons are typically formed in an electron transfer process from an alkali metal into an unoccupied anti-bonding π^* orbital of the aromatic hydrocarbons. In the Birch process, the creation of aromatic radical anions is considered the first crucial step before subsequent protonation reactions take place,[4] facilitated by suitable proton donors (typically alcohols). While the classic Birch reduction is conducted in liquid ammonia, various approaches have been pursued recently to identify solution and solvent environments where Birch reduction may be performed at room temperature.[5,6] Search for new solvents for the Birch reduction process is driven also by the fact that in contrast to liquid ammonia most organic solvents typically do not accommodate solvated electrons in large enough concentrations for extended periods of time, or they even directly react with the dissolved electrons. While numerous studies have explored the stability of aromatic radical anions in the gas phase,[7–10] binding energies of the valence electrons of polycyclic aromatic rad-

[a)] Electronic mail: stephen.bradforth@usc.edu

[b)] Electronic mail: hanns_christian.schewe@uochb.cas.cz

ical anions in the solution phase are hitherto unexplored. Understanding the electronic structure of both the neutral aromatic systems and the corresponding radical anion species may be instrumental in proposing new solvent environments for Birch-like reactions and for understanding the stereochemistry of the resulting product species.[11]

The naphthalene radical anion (Np^-) and the benzophenone radical anion (Bp^-) are two prototypical aromatic hydrocarbon anions that are of general interest for many chemical processes. First, they are used as reductive compounds in specialized synthesis, e.g., in the pharmaceutical industry[12] since they form up to molar concentrations of both the anionic and the neutral species (naphthalene (Np) and benzophenone (Bp)) in many different solvents. Second, their radical anions are stable for hours if the temperature-stable experimental setup is kept under oxygen- and water-free conditions. Beyond organic chemistry, both species are intriguing subjects to study solvation phenomena; while both Np^- and Bp^- are stable anions in solution, only Bp^- forms a stable radical anion in the gas phase,[7] while Np^- occurs only as a metastable shape resonance.[13] The reactivity of both radical anions has also been quantified by determining their reductive potentials using cyclic voltammetry (CV) in tetrahydrofuran(THF).[1]

To investigate the electronic structure of the above systems, we employ the liquid micro-jet (LJ) technique in conjunction with X-ray photoelectron spectroscopy (PES), which enables direct measurement of the electronic structure of volatile solutions.[14–16] This method is well established for water and aqueous solutions, while extensions to cryogenic and non-polar liquids such as liquid argon and methane or most recently liquid ammonia and benzene solutions have been accomplished.[17–19] The peaks in the measured spectra correspond to the vertical detachment energies (VDEs) of both the solvent itself and the solute species. VDEs represent the vertical ionization energies of electrons probing the initial equilibrium state of the studied systems.[20] For radical anionic species, the lowest VDE corresponds to ionization from the singly occupied molecular orbital (SOMO). Moreover, LJ-PES is inherently sensitive to changes in the solute charge states,[21,22] identified by electron binding energy (eBE) shifts or changes in the peak shape of the valence band (VB) and core-level spectral features. From the onsets of the liquid's HOMO or SOMO spectral features we can estimate the adiabatic detachment energies (ADEs), enabling the quantification of reductive potentials for neutral or anionic solutes and relating thus to their chemical reactivity.

In the present work, we report LJ-PES measurements and electronic structure calculations of Np and Bp as well as their radical anionic counterparts of Np^- and Bp^- in the solvent environment of THF. The electronic open-shell character of the anionic species gives rise to a number of challenges. First, the initial state and final state contributions to the eBEs lead to separated features in the PE spectra which require a detailed analysis and assignment of the measured PE spectral features. Second, the electronic structure calculations of the photoionization energies require multi-reference approaches to accurately grasp the complex nature of the excess electron being delocalized over the conjugated systems.[23]

The paper is structured as follows. We characterize pure liquid THF for the first time to quantitatively determine the electronic structure of a solvent that is heavily used in organic synthesis. This is done by using LJ-PES in combination with ab-initio molecular dynamics (AIMD) simulations followed by G_0W_0 calculations. Next, we establish the electronic structure of Np/Np^- and of Bp/Bp^- in THF. We determine accurately their VDEs employing recently developed protocols.[24–26] Accompanying electronic structure calculations enable us to model the experimental PE spectra of these species in order to investigate solvent effects and to perform a proper orbital assignment of the measured PE features. Moreover, the delocalization pattern of the excess electron and the gas-liquid shift from the theoretical calculations provide us with insights into the mechanisms leading to the stabilization of these radical anions upon solvation. In this context, the Np/Np^- systems are discussed in relation to our previous computational on benzene and its radical anion (Bz/Bz^-).[27,28] Finally, we compare the reductive potentials extracted from the present LJ-PES measurements with literature values from CV measurements,[1] which allows us to relate directly to the chemical reactivity of these radical anions in solution.

2. METHODS

Experiments

The experimental procedures consisted mainly of three parts: solution preparation, conduction of LJ-PES measurements and data-analysis. We will only summarize the relevant parts while a much more detailed description and characterization is given in the SI.

Tetrahydrofuran (THF) solutions were prepared in a stepwise manner: firstly, THF was purified using a destillation unit common in organic laboratories. Secondly, defined amounts of solid naphthalene (Sigma Aldrich, 99%) or benzophenone (Sigma Aldrich 99%) were dissolved in the purified THF. To generate the radical anion solutions potassium (Sigma Aldrich, 98%) was added in excess underneath an argon atmosphere. The radical anion solutions were filtered in a nitrogen glovebox before they were transferred to the cryostat unit under air-tight conditions for measurements.

The left part of Figure 1 depicts the cryostat unit which encases the sample cylinder in a cold ethanol bath which is cycled by a commercial chiller unit, thus, kept at a constant temperature of ≈273 K. Liquid microjets were routinely generated by applying pressure of 2-3 bar of argon at the head-space of the sample cylinder which pressed the solutions into a vacuum via a quartz capillary (inner

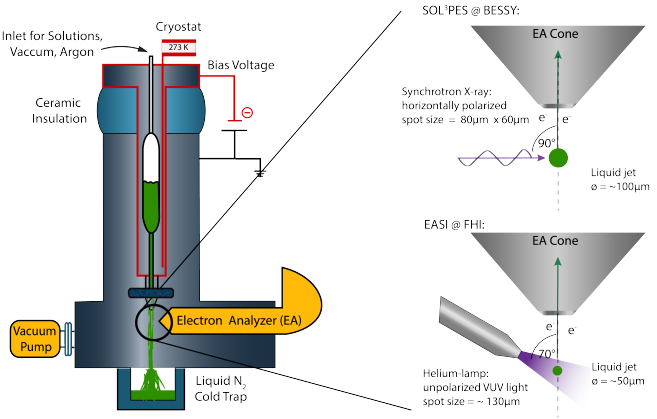

Figure 1: Sketch of the experimental setup.

diameter of 50μm), which was affixed to the outlet of the filter. The cryostat unit is mounted on top of a ceramic flange, ensuring electric insulation of the cryostat unit and thus the liquid jet to the main instrument. Moreover, using a power supply (Delta Elektronika) enabled the application of a bias voltage U between the liquid jet and the electron analyzer generating an electric field that accelerates the photo-electrons toward the hemispherical electron analyzer.

We performed LJ-PES measurements at the two different instruments, firstly at the U49/2-PGM-1 beamline[29] at the BESSY II electron storage ring operated by the Helmholtz-Zentrum Berlin für Materialien und Energie abusing the SOL^3 PES setup.[30] The right upper part of Figure 1 depicts the assembly geometry shown from the top perspective: the LJ runs vertically downwards while the linearly polarized X-ray beam (polarization axis is in the horizontal plane) illuminates the LJ in 90°. Photoelectrons (PE) were measured using a HiPP2 (SCIENTA) hemispherical analyzer mounted in the horizontal plane in 90°relative to the LJ and 90°to the X-ray beam.

Valence band PE spectra were first recorded at BESSY-II with a photon energy of hν = 123.464 ± 0.004 eV with an overall instrumental energy resolution of 30 meV (FWHM) determined by the convoluted uncertainty of the electron analyzer (25 meV) and the beamline (16 meV). The photon energy of the beamline was calibrated on a daily basis by measuring an electron-yield X-ray absorption spectra generated by the integration of the electron emission arising from the 2p3p3s Auger decay channel of an argon resonance at hν = 246.928 ± 0.004 eV. For calibration we used the 10% contribution from the respective second harmonic light (hν = 246.928 eV) present additional to the fundamental hν = 123.464 eV. The beamline exit slit defined the rectangular shape of the 40 x 60 μm^2 (horizontal x vertical) X-ray spot size.

For reproducibility, measurements were later conducted using the EASI setup[31] at the Fritz-Haber Institute (FHI) of the Max-Planck Society. The lower right part of Figure 1 depicts the geometry used at FHI: the liquid jet runs vertically downwards in 90°to the horizontally mounted Helium plasma light source and the hemispherical electron analyzer (HiPP3 SCIENTA) while the angle between the latter two components is 70°.

The VUV helium plasma lamp emitted unpolarized light which is supplied through a monochromator and a quartz capillary. The He-II α line provided a photon energy of hν = 40.814 ± 0.002 eV, where the intrinsic width of the atomic line determines the uncertainty. The beam spot size was determined at the point of incidence with the liquid jet and had an approximate diameter of 300 x 300 μm^2. Using a pass energy of 20 eV, the hemispherical analyzer resolution was found to be about 40 meV.[24]

In order to separate the liquid phase PEs from the gas phase ones, a negative bias voltage U (-50 V for SOL^{3}PES and -25 V for EASI) was applied. This enables to perform an absolute binding energy calibration procedure[24,32] by recording the spectral features of the valence band as well as the low-energy tail (LET) curve. These protocols[24] allow the determination of the binding energies to be consistent across different measurements despite certain parameters – such as the photon energy or the effective bias voltage – might change.

Electronic Structure Calculations

A. Ab initio molecular dynamics and G_0W_0 calculations

A configurational sampling of the geometries of the THF molecule in the gas phase at a constant temperature of 300 K was obtained through a classical *ab initio* molecular dynamics simulation using the CP2K software, version 2022.1.[33] The electronic structure was solved on the fly using the Quickstep[34,35] DFT module of CP2K. We used the revPBE0-D3 hybrid density functional[36–39] to represent the valence electrons and the Goedecker–Tetter–Hutter pseudopotentials[40] to represent the 1s core electrons of carbon and oxygen atoms. The Kohn–Sham orbitals were expanded into the TZV2P-GTH basis[34] set and, at the same time, a plane-wave basis with a 600 Ry cutoff was used to represent the electron density. The system was described in open boundary conditions, which was achieved by centering the molecule in a 12 Å wide cubic box and employing the Possion wavelet solver for electrostatic interactions, as implemented in CP2K. In addition, we employed the auxiliary density matrix method[41] with a pFIT3 fitting basis set to accelerate our calculation. The atomic nuclei were propagated for a total simulation time of 10 ps using the Verlet propagator and an integration time step of 0.5 fs. Canonical conditions were imposed using a local stochastic velocity-rescaling thermostat[42] with a time constant of 50 fs.

For the G_0W_0 calculation,[43] which is used to access physically meaningful one-electron binding energies to model the electronic density of states, we selected a subset of *ab initio* molecular dynamics geometries regularly

separated in time by a stride of 10 fs. The calculations of the G_0W_0 energy corrections were performed again using CP2K and started from Kohn–Sham orbitals obtained with identical electronic structure settings as the *ab initio* molecular dynamics simulation. Specifically, we use the eigenvalue-self-consistent version[43] of G_0W_0 (evGW), which provides iterative corrections building on the self-consistency of the energy eigenvalues only, without changing the corresponding one-electron states. The calculation was accelerated using the resolution of identity approach with the RI-TZ auxiliary basis and further relied on the Padé approximation to analytically continue the self-energy on the real frequency axis and the Newton-Raphson fixed point iteration to numerically solve the relevant algebraic equations. The evGW energy corrections were calculated for all occupied orbitals and additional 10 virtual orbitals. The resulting corrected quasiparticle energies were binned into a histogram with a 0.10 eV bin width over the range of −35 to −5 eV to represent the electronic density of states (EDOS).

B. Modeling photoelectron spectra and ionization energies of aromatic radical anions

In this study, we calculated the lowest ionization energy (corresponding to ionization from the HOMO orbital for the neutral species and the SOMO orbital for the anionic species) as the energy difference between the ground states of the initial and ionized species. For higher ionization energies, we calculated the energy difference between the ground state energy of the initial species and the excited states of the ionized species.[44]

Within our previous studies, we analyzed the aromatic radical anion of benzene using the density functional theory (DFT) and the perturbative Moller-Plesset (MP2) methods.[45,46] However, these single reference approaches were insufficient for a correct description of naphthalene radical anion and benzophenone radical anion. In particular, calculations revealed a multireference character of the investigated radical anions, as also manifested by high spin contamination of the MP2 results.

Given also the need to account for excited states for evaluating higher ionization energies and the fact that multireference-based approaches can in principle provide an accurate description thereof, we have opted to employ Complete Active Space Self-Consistent Field (CASSCF)[47] calculations using the ORCA 5.0.3 program package.[48,49] These multireference calculations revealed that for the naphthalene radical anion, the leading configuration accounted only for 84 % of the ground state. For the ground state of the benzophenone radical anion, the multireference character was even more pronounced (77 % contribution of the leading configuration).

Solvent effects were included in the form of a structureless medium within the integral equation formalism of the polarizable continuum model (IEF-PCM).[50–52] For a proper treatment of the solvation effect on fast photoionization processes, we employed the non-equilibrium PCM (NE-PCM) approach,[53,54] which accounts for a partial relaxation of the PCM cavity charges due to the high-frequency component of the dielectric constant only ε_∞.

The neutral and anionic structures were first preoptimized in a PCM of tetrahydrofuran using the B3LYP hybrid DFT functional[55] equipped with the D3BJ dispersion correction[56,57] employing the aug-cc-pVTZ[58] basis set. These structures were then used for gas-phase single-point CASSCF calculations. The final gas phase single-point energies for ground states of parent and ionized species, as well as for the first five excited states of the ionized species were obtained using the SC-NEVPT2 perturbation[59–61] over CASSCF with the same basis set. The low ionization potential region of aromatic compounds typically includes only π-electron ionization bands.[62] Therefore, the π molecular orbitals (MOs) were included in the complete active space for the CASSCF calculations, resulting in a CASSCF-(10-10) active space for Np and CASSCF-(11-10) for Np^-. In the same manner, the active space for Bp included all the 14 π MOs, resulting in CASSCF-(15-14) for Bp^- and CASSCF-(14-14) for Bp.

The solvation energy for each of the investigated aromatics was evaluated at the B3LYP/aug-cc-pVTZ[58] level of theory with the D3BJ dispersion correction,[56,63] employing the non-equilibrium PCM (NE-PCM) formalism as implemented in the Gaussian16[64] program package. We calculated the solvation energy of the parent structure before ionization by taking the difference between the energy of the optimized parent species in the THF PCM model and the gas-phase energy of the same structure without any geometry relaxation. To obtain accurate values of the solvation energies, the calculations were performed separately for each of the studied excited states. It is important to note that since no geometry relaxation occurs during photoionization, we performed all calculations on the same pre-optimized geometries of the initial species before ionization, employing PCM of THF. The obtained CAS-SCF gas-phase photoionization energies were then shifted by the corresponding gas-liquid shift obtained separately for each of the states.

3. RESULTS

Characterization of the solvent THF

In order to characterize the valence band electronic structure of the solvent THF we first investigate THF in the gas phase. This enables us to relate our findings to previous investigations by adopting, *e.g.*, orbital assignments from the gas phase to the liquid phase. It also allows us to determine the gas-to-liquid peak shift which informs on the effect of solvation on the ionization process and whether there are any differential shifts between different molecular orbitals.

The central panel of Figure 2 depicts the gas-phase

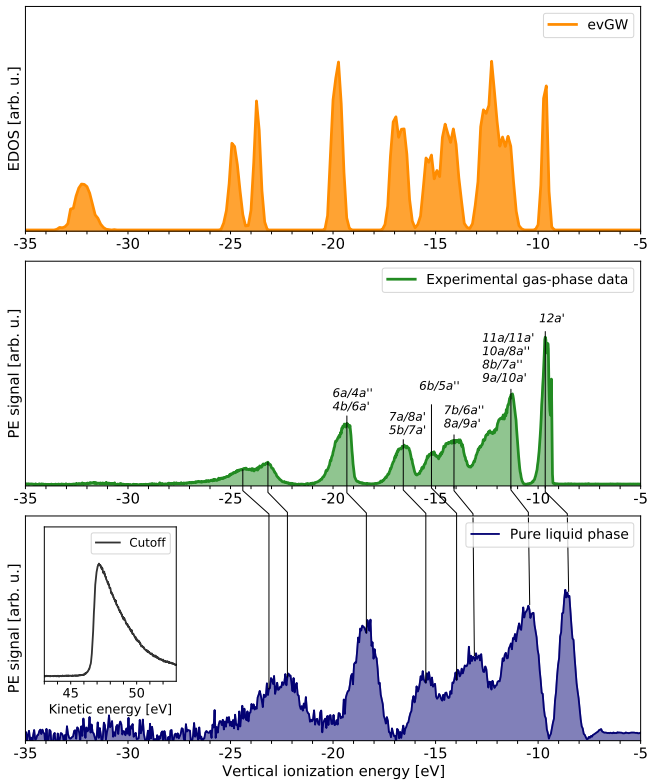

Figure 2: Valence band spectra of THF. (Upper panel) electronic density of states calculated using evGW. (Central panel) gas-phase photoelectron spectrum of THF. Assignments are from ref.[65](Lower panel) liquid-phase photoelectron spectrum of THF with a salt concentration of 0.1 mol/L $TBA^+PF_6^-$. By applying a bias voltage of U =-50 V the low electron energy cutoff is measured (inset) together with all valence band spectral features of interest. Experiments were conducted at the BESSY II synchrotron.

PE spectrum of THF recorded using the SOL^{3}PES instrument at BESSY II. We moved the liquid jet out of the synchrotron light beam such that only THF molecules that had evaporated from the liquid surface were ionized. The binding energy of the spectrum has been calibrated using the gas-liquid phase spectrum shown in the supplementary information. Following reference 65, we assigned the spectral features to MOs from which ionization takes place as a function of increasing binding energy. The peak positions of the individual spectral features (stated in Table 1 of the SI) are in good agreement with prior experimental work which also considered ionization to be approximately 20 eV above the first IP.

The gas-phase THF experimental peak positions are closely reproduced by evGW calculations, as shown in the top panel of Figure 2. Intensities of the spectral features differ between the experiment and the theory as the calculation at this instance examines the EDOS without any reference to experimental cross sections; unlike the experimental spectrum, the calculated EDOS integrates to the number of states. The THF molecule is known to exhibit an out-of-plane ring puckering deformation which allows the existence of two unique potential energy minimum geometries that can be switched between each other through a pseudo-rotational motion. Giuliani et. al.[66] identified the two conformations of C_2 (twisted) and C_s (envelope) symmetries and estimated their simultaneous populations at 298 K at a ratio of 0.55 to 0.45, respectively. Consistently, our AIMD trajectory samples frequent transitions between the corresponding potential energy wells, which implies low barriers for the process. As such, the calculated EDOS takes into account these deformations, and the data shown in Figure 2 represents the average density of states over all possible, thermally available geometries. This is also the case with the experimental spectrum. In principle, it might be expected that one could use the insight offered by the calculation to obtain the individual contributions to the spectra originating from the individual potential wells surrounding the equilibrium conformers. However, it is shown in Section 2B of the SI that there is very little variation in the EDOS curves for different THF conformers within the available statistics.

The lower panel of Figure 2 depicts the liquid-phase spectrum (black line) from a pure liquid THF microjet with a salt concentration of 0.1 mol/L $TBA^+PF_6^-$. When comparing the gas phase valence band spectrum to the liquid phase data, we observe that all spectral features show practically the same binding energy shift of $\approx$ 1.3 eV compared to their gas phase counterpart – a detailed and individual comparison is given in Table 1 of the SI. The shift is graphically displayed in Figure 2 by the displaced vertical black lines connecting each individual valence band peak from the gas phase spectrum (central panel) to its corresponding peak from the liquid-jet PE spectrum (lower panel). In addition, we notice a small broadening of $\approx$ 0.1 eV due to the solvation of the already vibronically-broadened spectral features.

By applying a bias voltage of U =-50 V we employ the protocols to determine absolute binding energies by measuring the low kinetic energy cutoff as well as all spectral features of interest.[24,26,32] Thus, we determine the vertical ionization energy (VIE) of the liquid HOMO of THF to be $\mathrm{VIE}_{\mathrm{liq}}^{\mathrm{THF}} = -8.45 \pm 0.1$ eV, while the averaged literature value for the gas-phase is $\mathrm{VIE}_{\mathrm{gas}}^{\mathrm{THF}} = -9.71 \pm 0.03$ eV,[65,66] resulting in a gas-liquid shift of $\Delta\mathrm{BE}^{\mathrm{THF}} = 1.28$ eV. For comparison, we apply a Born-Haber cycle [26] to provide a continuum estimate for the gas-liquid shift $\Delta\mathrm{BE}_{\mathrm{BH}}^{\mathrm{THF}}$ for ionizing a neutral THF molecule in a solvent of THF. We employ the high-frequency dielectric constant ε_r given by the square of the refractive index $\varepsilon_r = n^2 = (1.401)^2$ [67] and an average molecule-molecule distance of 5.25 Å [68] in the liquid phase. This results in a gas-liquid shift value of $\Delta\mathrm{BE}_{\mathrm{BH}}^{\mathrm{THF}} = 1.36$ eV which agrees well taking into account that the THF structure deviates from a sphere.

Experimental spectra of Np/Np$^-$ and Bp/Bp$^-$ in THF

Gas phase Np has a VDE of -8.144 eV,[73] while its EA is negative when isolated in vacuum. On the other hand, the negative ion Np$^-$ is known to be stabilized in the weakly polar solvent, THF, giving a strongly colored green solution. Bp has higher ionization energy in the gas phase but supports a stable negative anion Bp$^-$ in a vacuum with a VDE between -0.7 to -1.0 eV.[74] However, the binding energies of the valence electrons in these or any other simple polycyclic aromatic anion in the solution phase are hitherto unknown.

Figure 3 compares the PE spectra of the neutral aromatics Np and Bp (right panels) with those of the corresponding radical anions Np$^-$ and Bp$^-$ (left panels), all in THF. In all data sets, the highest binding energies peak at $\mathrm{VIE}_{\mathrm{liq}}^{\mathrm{THF}}$ = -8.45 ±0.1 eV are from the THF solvent, as discussed above. For the neutrals, the lowest binding energy peak should arise from ionizing the solute HOMO, giving rise to a spin doublet cation and a single additional assignable peak. This is the typical situation for PE spectra for closed-shell singlet species, like Np or indeed the solvent THF, as the only selection rule in PES is connecting configurations by the removal of a single election. Thus, only spin doublet final states can result. We only clearly see an additional peak for Np's HOMO. A similar concentration Bp solution provides a spectrum that shows only the same features as seen for neat THF. From these data, we can derive only the solution phase VIE for NP, $\mathrm{VIE}_{\mathrm{HOMO}}^{\mathrm{Np}}$ = -7.18 eV, almost 1 eV lower than the gas phase. The absence of a resolvable PE feature for the Bp HOMO might be expected based on the gas VIE lying at 9.05 eV,[75] some 0.6 eV higher than naphthalene's gas phase IP.

The PE spectra for the open shell Np$^-$ anion in Figure 3 are generated by the use of potassium metal on THF solutions of Np. The spectrum is recorded using He-II α radiation at 40.814 eV. In addition, we show in the SI Figure 4 the PE spectrum recorded with the SOL^{3}PES apparatus at BESSY with 123.464 eV photons when sodium/potassium alloy, sodium, or lithium metal is used as the reducing agent. In all spectra, three weak but reproducible peaks are observed in experimental spectra, with the data from both BESSY and FHI showing the lowest energy peak around -2.7 eV.

Unlike the fully occupied orbitals, photoemission from the singly occupied molecular orbital (SOMO) from the spin doublet anion can only lead to Np neutral in a spin singlet configuration. Thus, the binding energy peak at -2.7 eV corresponds to the lowest energy configuration of Np, namely the closed-shell singlet (S_0) ground state. This peak therefore determines the $\mathrm{VDE}_{\mathrm{SOMO}}^{\mathrm{Np}^-}$ = -2.73 eV of Np$^-$.

For every other fully occupied orbital in the anion, we would expect two PE peaks separated by the singlet-triplet splitting for the neutral Np configuration associated with the removal of this electron. So, in removing an electron from the first fully occupied orbital, the final states will be the excited singlet (S_1) and triplet (T_1) states of neutral Np. The 0-0 origin for the T_1-S_0 transition lies at 2.64 eV in hexane solution as determined by oxygen-sensitized absorption.[70] This suggests the assignment of the second lowest-lying peak (at -5.26 eV eBE) in Figure 3 (top left) as a detachment to T_1. We can use the well-known optical spectra for solution phase Np, from its ground and lowest triplet states,[70] to establish a ladder of expected final states, and this is the ruler shown in the top parts of anion spectra in Figure 3. This procedure suggests an assignment for each peak observed, as well as identifying when the photodetachment features give way to lying hidden behind the more intense features due to ionizing THF. Comparisons to theoretical evaluation will provide further evidence to expand upon this assignment including the molecular orbitals involved.

The comparison of Np$^-$ solution PE spectra shown in the SI shows two interesting additional details: The first is that while the two lowest binding energy peaks are well reproduced when different spectrometers and radiation sources are used, in the region close to the first THF ionization feature, the third peak seems more pronounced when recorded with 40.8 eV radiation and a fitted peak center at -7.4 eV is closer to the onset of electrons ejected from THF than the experiment where $h\nu$ = 123 eV radiation is used. Given the possibility for multiple PE peaks in this region (see optical spectra ladder in Figure 3 and calculations below), our current understanding is that different PE angular distributions, as well as different energy-dependent cross sections for each of the overlapping detachment transition, are giving rise to the difference in appearance in this region. We note that the Helium lamp is unpolarized and the synchrotron radiation is linear horizontally polarized with respect to the electron detection direction.

Secondly, it has been established that ion pairing takes place between aromatic anions and the alkali metal cations in solution, especially for solvents with small static dielectric constants.[1] It has been observed for Np$^-$ in solution that the probability for contact ion pairing increases with the size of the alkali metal cation - thus it is more likely for K^+ to pair with Np$^-$ than for Na^+ and even less for Li^+. However general rules for ion pairing also consider the softness of the anion [ref], based on polarizability. For example, for Bp$^-$ the tendency for ion-pairing is reversed; it is observed that ion pairing is likely for Li^+ than for Na^+ and even less for K^+. An interesting question is therefore whether the binding energy is sensitive to the cation location in the first solvent shell, as is observed for more polar solvents like water.[ref] While we observe no peak shifts for solutions of Np$^-$ with alkali metal cations generated from solid K and Na metal as well as NaK alloy, there may be an indication (albeit weakly supported at this point) for noticeable peak shifts in preliminary recorded data from solutions generated from lithium reduction of Np as we discuss further in the SI.

We have also recorded the PE spectra for Bp$^-$ in THF.

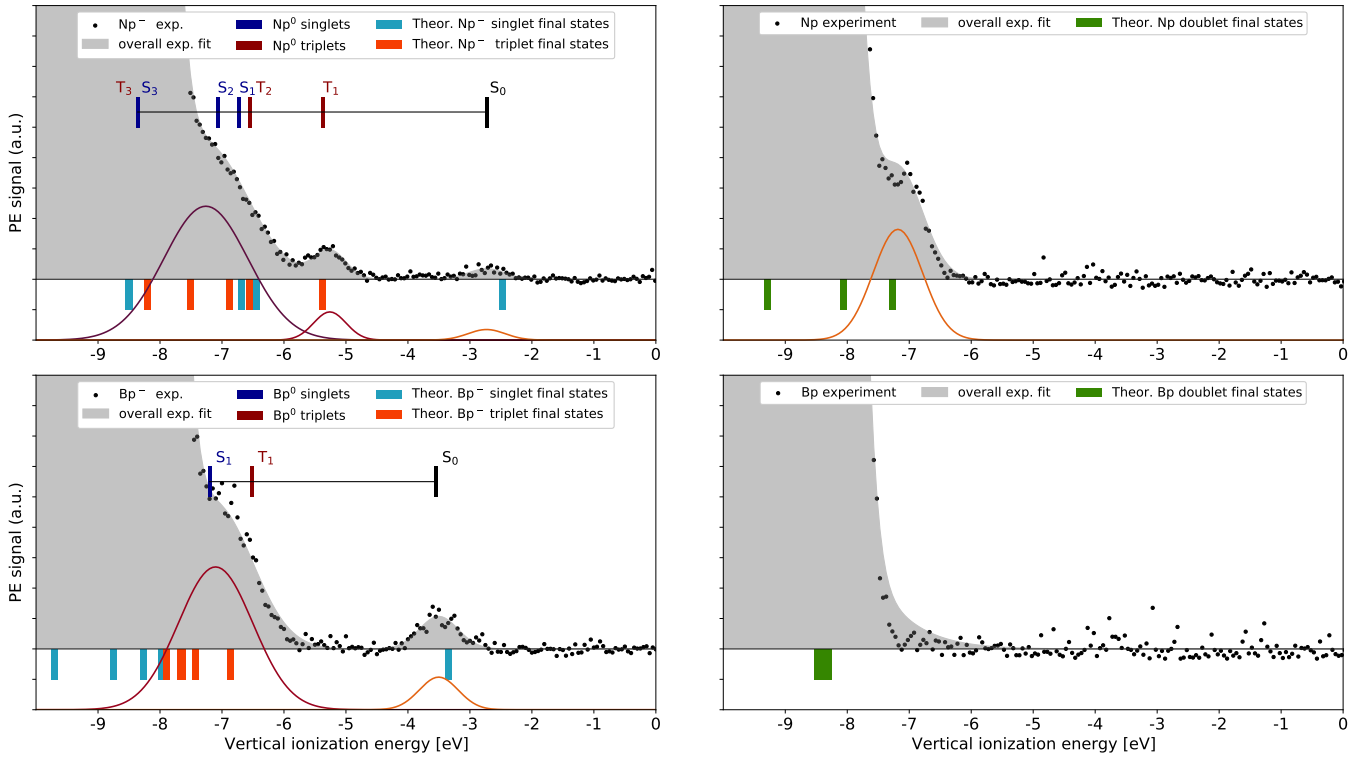

Figure 3: Experimentally measured PE spectra (dots) for neutral and radical anion aromatics dissolved in THF. The top panel shows the valence band spectra of the naphthalene radical anion (Np^-) (left) and neutral naphthalene (Np) (right) in THF; the bottom panel provides the spectra of the benzophenone radical anion (Bp^-) (left) and neutral benzophenone (Bp), respectively. Also shown in each panel are fits to the experimental data; the overall best fit is shown by the grey background with underlying component Gaussian curves shown below, colored to match column labels in Table 1, where peak center values are provided. The theoretical photoionization energies calculated here are shown below each dataset (cyan and orange bars). To aid in the assignment of the radical anion data, the spectroscopic origins (refs. 9,69–72) for the low-lying triplet and singlet final states of the corresponding neutral aromatics are shown by a ruler; each spectroscopic origin is referenced to S_0 centered at the experimental position for the observed removal of the SOMO from the respective radical anion.

Figure 3 (bottom left) shows clear evidence for a much more strongly bound excess electron in the Bp^-. Once again, if Bp^- is a doublet, detachment from the SOMO should lead to a single final neutral state, whereas transitions arising from fully occupied orbitals will lead to a pair of transitions separated by the exchange interaction. The lowest lying detachment peak, at -3.55 eV binding energy, corresponds to the Bp^- SOMO. A ladder of energies is shown above the PE data derived from optical spectra of Bp in the singlet and triplet manifolds. The neutral Bp T_1 energy relative to the ground state S_0 (e.g., 2.97 eV[71] is well known because of its widespread use as a triplet photo-sensitizer.[8] The S_1-T_1 splitting is smaller for Bp (S_1 at 3.65 eV in hexane)[72] than Np and it appears that the broad and more intense peak observed in Figure 3 at -7.15 eV does not resolve the singlet-triplet splitting. Our calculations below expand on the location of the higher-lying states.

In the SI, we compare the relative advantages of synchrotron- versus lab-based valence-band photoelectron (PE) measurements. There we examine the signal-to-noise ratio (SNR) as well as consider the contrast relative to the background in the baseline region required to establish the energies for ejection from the weakly bound orbitals of the anion. Because non-resonant PE spectroscopy has equivalent sensitivity to a solute or solvent molecule, it is always a challenge to collect high SNR data to examine the solute electronic structure, even for moderately concentrated solutions. For highly reactive solutions in liquids that form less stable jets like THF, this is additionally challenging. We conclude that the absence of higher harmonic radiation with the helium lamp radiation source is an advantage providing a cleaner baseline in the lower binding energy region, while still providing high enough photon energies to avoid a large low energy tail from inelastic scattering. With the longer run times possible in a small lab setting, data with comparable SNR is achievable despite the lower light fluxes compared to the synchrotron.

Peaks	$HOMO_{THF}$	1st	2nd	3rd	instrument/method
pure THF	−8.45				BESSY/FHI
	−8.45				G_0W_0
Np	−8.45	−7.18			FHI
		−7.28 (HOMO)			CASSCF
Np^-	−8.49	−2.73	−5.26	−7.26	FHI
		−2.48 (SOMO)	−5.37 (HOMO)	−6.44 (HOMO)	CASSCF
				−6.56 (HOMO−1)	CASSCF
				−6.69 (HOMO−1)	CASSCF
				−6.88 (HOMO−2)	CASSCF
Bp	−8.45				FHI
		−8.30 (HOMO			CASSCF
		−8.35 (HOMO−1)			CASSCF
		−8.38 (HOMO−2)			CASSCF
Bp^-	−8.45	−3.55	−7.15		FHI
		−3.34 (SOMO)	−6.86 (HOMO)		CASSCF
			−7.43 (HOMO−3)		CASSCF
			−7.64 (HOMO−1)		CASSCF
			−7.66 (HOMO−2)		CASSCF
			−7.98 (HOMO−3)		CASSCF

Table 1: Overview of vertical detachment energies (VDEs) of the studied systems. The first column denotes the investigated system. The second to fifth columns present the spectral characteristics of the liquid HOMO of THF, followed by the third, second, and first peaks of the solute associated with solute orbitals. Experimentally determined VDEs are displayed in black, while theoretically calculated VDEs are denoted in blue for singlet, green for doublet, and red for triplet final states. The MO contributing the most to the photo-emission intensity is indicated within brackets for each theoretical value. Note: the other MOs contributing as well as their orbital labeling is listed in detail in the SI. The last column states where the experiment has been conducted.

Simulation of the Np/Np^- and Bp/Bp^- photoemission

With the range of experimental observations now described and an empirical assignment in place, we will move on to employ detailed electronic structure calculations for Np^- and Bp^- to more fully interpret the measured spectral features in PE spectra depicted in the left panels of Figure 3.

Np^- possesses a D_{2h} symmetry in its ground state with a calculated electron configuration of: ... $\pi(b_{1u})^2$ (HOMO−4), $\pi(b_{2g})^2$ (HOMO−3), $\pi(b_{3g})^2$ (HOMO−2), $\pi(a_u)^2$ (HOMO−1), $\pi(b_{1u})^2$ (HOMO), $\pi^*(b_{2g})^1$ (SOMO). The unpaired excess electron resides in the $(b_{2g})^1$ singly occupied molecular orbital (SOMO) as shown in the upper part of Figure 4. A table with all π molecular orbitals of naphthalene radical anion can be found in the Supporting Information (Figure 11). The distribution of the spin density describing the delocalization of the excess electron is shown in Figure 6 of the SI. The removal of the SOMO to give rise to S_0 is shown with a blue line at -2.48 eV (Figure 3, the bottom panel with calculated photodetachment energies).

The removal of an electron from the doubly occupied b_{1u} (HOMO), results in the singlet (S_1) or triplet (T_1) state of the neutral. Likewise, because electron removal from any lower-lying MO results in a pair of singlet and triplet final states, we have indicated these pairs in blue and red, respectively, in Figure 3. Table 1 lists all calculated VDEs contributing to a measured spectral feature while the initial MO prior to emission is stated in brackets as well as the final state singlet and triplet character is indicated by the blue and red coloring.

Bp^- on the other hand has a C_2 symmetry in its ground state with a calculated electron configuration of: ... $\pi(1b)^2$ (HOMO−6), $\pi(1a)^2$ (HOMO−5), $\pi(2b)^2$ (HOMO−4), $\pi(3b)^2$ (HOMO−3), $\pi(2a)^2$ (HOMO−2), $\pi(4b)^2$ (HOMO−1), $\pi(3a)^2$ (HOMO), $\pi^*(5b)^1$ (SOMO). The unpaired excess electron resides in the $(5b)^1$ SOMO shown in the bottom part of Figure 4, while Figure 11 of the SI depicts all π MOs of Bp^-. The spin density of the excess electron can be found at the bottom panel of Figure 6 in the SI.

Ejection of the single electron from the SOMO results in the singlet ground state (S_0) for neutral Bp; our calculations provide for Bp^- a $VDE_{SOMO}^{BP^-}$ = -3.34 eV, close to the measured peak VDE. The removal of an electron from the doubly occupied 3a (HOMO) results in either the lowest excited energy singlet (S_1) or triplet (T_1) state of neutral Bp and removal from any lower-lying MO results in further pairs of neutral singlet or triplet final states, which are indicated blue and red, respectively, in the lower part of Figure 3. In analogy to Np^-, the lower part of Table 1 lists all calculated VDEs of Bp^- contributing to a measured spectral feature while the initial MO prior to emission is stated in brackets. The final state singlet and triplet character is indicated by the blue

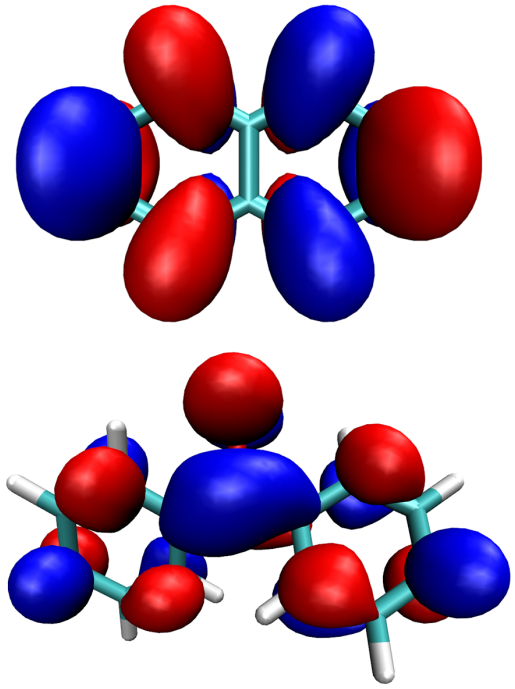

Figure 4: SOMO of naphthalene radical anion (top) and benzophenone radical anion (bottom) plotted with an isovalue of 0.025 $a_0^{-1.5}$.

and red coloring as well. Our calculations reveal that the second detachment feature for Bp^- is quite complicated, arising from four triplets and one singlet final state. This accounts for the significantly larger area under this peak compared to the $VDE^{BP^-}_{SOMO}$ = -3.5 eV.

Gas-liquid solvation shift

Table 2 summarizes the gas-liquid solvent shift ΔG_{DFT} estimated from electronic structure calculations using non-equilibrium PCM models. The VIEs of the neutral aromatics are predicted to be smaller compared to the gas phase by 0.90 - 0.95 eV for Np and 0.74 - 0.86 eV for Bp, respectively. This VIE decrease is similar (but smaller) compared to the one observed for THF itself. In simplest terms, the aromatic molecule being ionized is somewhat larger, and so the solvation energy for the final state cation is correspondingly reduced. On the other hand, for the anions, the effect of solvation on the VDE is much larger, ranging between 2.39 - 2.64 eV for Np^- and 2.09 - 2.44 eV for Bp^-. While an experimental value for the shift can not be evaluated for Np, comparing our liquid phase VDE to reference[74] for Bp^- suggests an experimental shift of 2.6 - 2.9 eV. This difference and its implications on the stability of aromatic radical anions in solution will be discussed further below.

The Born-Haber cycle can be used to rationalize the Gibbs free energy of solvation ΔG_{BH}. It accounts for the initial and final oxidation state of the species upon electron ionization or detachment during the photo-emission while details are given in the SI. This leads to two distinct cases:[26] (1) for an initial neutral species the final state is cationic: here, only the electronic part of the solvent relaxation needs to be accounted for during solute solvation. This is done by replacing ε_r with its high-frequency limit namely the square of the refractive index $\varepsilon_r = n^2 = 1.97$.[67] (2) for an initial anionic state the final state is neutral: here, ΔG is predominantly defined by the solvation of the anionic solute while the contribution from the final neutral is expected to be negligible. Thus the solvent polarizable continuum is given by its static dielectric constant which in THF exhibits a value of ε = 7.42.[67] Thus, the different initial oxidation states of the solute species interact with different parts of the dielectric constant, hence the difference in the solvation shift for neutral and anionic species.

	ΔG_{DFT}	ΔG_{DFT} range	ΔG_{BH}
Np	0.91	0.90 - 0.95	0.94
Np^-	2.47	2.39 - 2.64	2.66
Bp	0.74	0.74 - 0.86	0.78
Bp^-	2.28	2.09 - 2.44	2.27

Table 2: Solvent-induced shifts ΔG of the HOMO binding energies (first column) and range of solvent-induced shifts for all calculated binding energies (second column)(in eV) determined by electronic structure calculations (DFT) for the studied systems of Np, Np^-, Bp, and Bp^-. As a comparison, the last column lists the corresponding solvent shifts estimated using the classical Born-Haber cycle.

Estimating the reductive potentials and thermodynamic stability of Np^- and Bp^-

Consistent with our experimental ability to create and study stable solutions of these aromatic anions, the calculations confirm that these anion systems are quite robust to electron detachment having significant positive VDEs when dissolved in THF. While the VDE defines the stability of a species with respect to electron detachment upon absorption of ionizing radiation, the thermodynamic stability is of course determined by where the ADE of the anion lies. Thus, the ADE of a species in solution defines which species form and where equilibria lie: in our case, the aromatic anions compete with the formation of other species such as solvated electrons in THF or the precipitation of alkali metal. Figure 5 depicts the measured PE spectra of the solutes of Np^- and Bp^- and Ferrocene in THF, measured in separate experiments. We can use the spectra to evaluate the ADEs by estimating the onset at the low binding energy side of the lowest BE spectral feature following the pro-

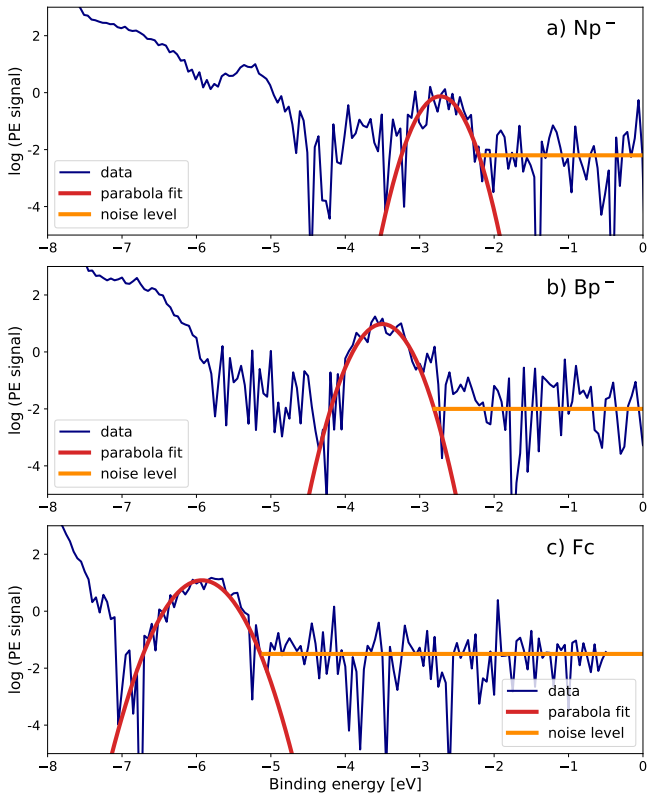

Figure 5: Estimation of reductive potentials relative to the Ferrocene standard. Panels a), b), and c) show the fits for the spectra of Np^-, Bp^- and Fc in THF.

cedures described in References . The logarithmic PE signal intensities as a function of the BE have been fit with a parabola, while the crossing point of the parabola with the noise level determines the onset value.[76] Thus, we determine, relative to vacuum, $^{(Np^-)}$ADE = 2.21 eV, $^{(Bp^-)}$ADE = 2.80 eV and $^{(Fc)}$ADE = 5.15 eV. Therefore, the PE spectra allow estimates of the reduction potentials, relative to a Ferrocene/THF standard as $E^0_{Np^-}$ = -2.94 eV and $E^0_{Bp^-}$ = -2.35 eV. These derived values agree very well with those determined by cyclic voltammetry (CV), namely $^{CV}E^0_{Np^-}$ = -3.1 eV and $^{CV}E^0_{Bp^-}$ = -2.3 eV, respectively.[1] The approach of self-consistently measuring ferrocene (Fc) also by liquid-jet spectroscopy avoids needing to apply literature estimates of Fc with respect to the vacuum level. It further provides confidence in our assignments and the solution identity within the liquid microjet.

4. DISCUSSION

In the following, we first discuss the general nature of an excess electron associated with two quite different aromatic radical anions and the implications of the PE characterization from this work. Secondly, we reflect on the mechanism that leads to an increase in the binding energy of the excess electron upon solvation effectively resulting in the stabilization of the radical anions. Finally, we follow up on the solvent-induced stability and its implications on the reactivity of radical anions as reactive intermediates within the Birch reduction process.

A. The electronic structure and nature of the solution phase radical anions

Neither Np^- nor the benzene radical anion (Bz^-) are stable species in the gas phase. Experimentally, however, the technique of electron transmission spectroscopy allows one to infer the vertical EAs of unbound resonant states, thus for Bz^- and Np^- the VEA_{Bz^-} = -1.15 eV, -4.85 eV and VEA_{Np^-} = -0.19 eV, -0.90 eV, -1.67 eV, -3.37 eV, -4.72 eV have been determined, respectively.[77] In contrast, anthracene radical anion (Ant^-) already possesses a positive $VEA_{Ant} = 0.53$ eV, thus being the smallest unsubstituted aromatic hydrocarbon forming a stable radical anion in the gas phase.[78] Similarly, benzophenone radical anion Bp^- is a stable compound already in the gas phase with a VDE of 0.91 eV [74] which is in good agreement with our theoretical computed value of VDE 1.07 eV. This difference in electron binding for Bp vs Np is largely because in the former case the excess charge is localized on a carbonyl anti-bonding orbital (Figure 4) rather than the ring π systems (but see below).

For the polyacenes, however, it is reasonable to ask how the extra electron becomes bound on introducing solvation? For Np^-, almost 3 eV of vertical stabilization for the excess electron is gained by immersion in the THF solvent. Does the environment simply provide electrostatic stabilization to the extra electron that is localized in a rather similar π^* LUMO as expected from gas phase electronic structure calculations? Or does the formation of a solvation shell extend the molecular entity such that it enables the wavefunction of the excess electron to delocalize into the solvent leading to a more stable molecular structure of the otherwise unstable anionic species? The latter would clearly have an impact on the reactivity of the radical anion, making it a much softer nucleophile. One might imagine the latter description of the excess electron as a hybrid between a solvated electron occupying interstitial space in the liquid and an orbital localized above and below the aromatic plane. We note that THF is known to have considerable excess space in the solvent network which is used to support excess electron density when excess electrons are generated by photodetachment or photolytic or radiolytic ionization.[13,68,79,80] A related question is whether the unoccupied orbitals in the solvent play a role by accepting part of the electron density, as occurs with excess electrons in ammonia and water ices, as implicated by EPR spectroscopy.[19,81–83]

Beyond measuring the VDE and the redox potential, we can compare our electronic structure calculations to molecular geometry and vibrational frequency data and

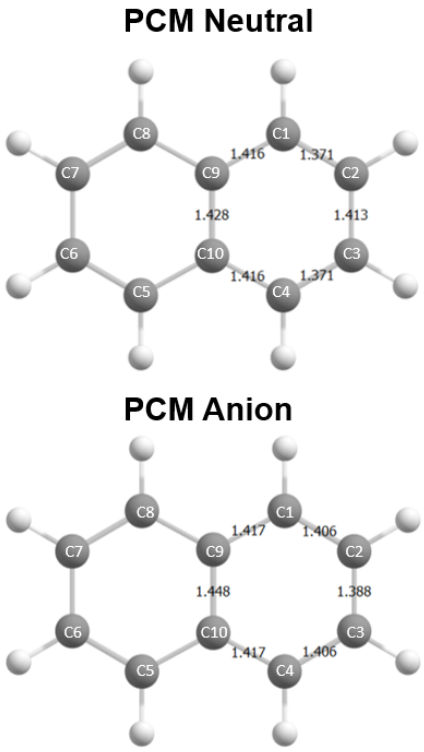

Figure 6: Theoretically predicted molecular geometry of neutral naphthalene and its corresponding radical anion in THF PCM model. A comparison of PCM structures with gas-phase structures can be found in the SI.

relate them to other polyacenes and their radical anions. The addition of an electron to the LUMO in D_{2h} aromatics has long been known to activate the bond alternation pattern in the C-C bond lengths in the molecular frame. For naphthalene, electronic excitation of the neutral molecule, promoting a $\pi^* \leftarrow \pi$ orbital, the bond order increases in C2-C3 and C6-C7 (shortening by 0.05 Å,[84] while decreasing in C1-C2 (and symmetry related C-C bonds) as well as the central C-C bond (elongating by 0.06 Å and 0.04 Å respectively - see Figure 6 for naphthalene carbon numbering). This can be understood in simple MO theory terms and by inspection of the nodal pattern in the HOMO and LUMO orbitals shown in Figure 11 in the SI. The change in the bonding pattern is sufficient to give a long Franck-Condon progression in the electronic absorption spectrum in the totally symmetric C-C framework stretching modes.[85,86]

In the removal of a SOMO π^* electron localized on the molecular anion, one would expect an oppositely signed bond alternation change, but not as dramatic in magnitude because an electron has not been changed in the π HOMO. Garand's gas phase high-resolution PE spectra report[87] detachment to the singlet and triplet states with equal footing, as is seen in our work. In their PE spectra, the origin is the most intense peak but there is again vibrational activity in the totally symmetric stretch modes, the modes allowed in PE transitions. Activity is observed in the totally symmetric framework vibrations (assigned as $\nu_6 = 1267$ cm^{-1} and $\nu_7 = 1416$ cm^{-1} in reference 87) while simulations of the Franck-Condon progressions are consistent with calculations presented in their paper that show a bond alternation change of 0.022 Å with a pattern consistent (lengthening C2-C3, shortening C1-C2 etc) with the qualitative expectations outlined above. The mean absolute C-C change is about half of that connected with the $\pi^* \leftarrow \pi$ excitation from $S_1 \leftarrow S_0$.[84] The PE spectrum also reveals a lesser degree of C-C frame activity in ν_6 and ν_7 induced on the removal of the π electron to reach T_1. Moving to the solution phase, Juneau et al.[88] report a significant (30-45 cm^{-1}) drop in the 1260 and 1400 cm^{-1} (ν_6 and ν_7) vibrational frequencies for Ant$^-$ compared to Ant in the measured resonance Raman spectra, consistent with the addition of an electron to a characteristic π^* orbital.

While we cannot observe vibrational progressions in the liquid phase PE spectroscopy because of solvent-induced broadening, our calculations present a picture matching the qualitative pattern described above for anthracene radical anion, where calculations and experiment provide a consistent description. Figure 6 shows a computationally predicted bond alternation in Np upon adding the excess electron characterized by lengthening of 0.02 Å in the C2-C3 and C7-C8 bonds and shrinking most notably of C1-C2 (and symmetry equivalent bonds) of 0.03 Å. One can anticipate that if an isolated molecular ion picture applies to Np$^-$ in THF, some of the width and peak shape observed in the $D_0 \leftarrow S_0$ PE band arises from Frank-Condon activity in this framework distortion. Because the calculations employ a polarizable continuum model, they cannot address whether the excess electron density is entirely localized in the π^* orbital. But we note that the continuum model does correctly predict the magnitude in the VDE shift from vacuum to THF and it is hard to see how this would happen if we had an entirely incorrect binding motif for the electron. More detailed multireference computations with explicit THF solvent molecules are too costly and methodologically demanding at the current time. But, as a further test that the excess electron is localized on the solute molecule and does not spread to the solvent molecules, we put one explicit THF molecule in the CAS-SCF calculations. This did not lead to any significant change in the spatial distribution of the spin densities on either anion (see Figure 7 in the SI for plots of the spin densities with an explicit solvent molecule).

B. Comparison to vibrational spectroscopy

We can explore this idea one step further by reviewing the IR and Raman spectroscopy of the solution phase Np$^-$ anion in THF.[89–91] Just as for Ant$^-$, a downshift in the three a_g C-C stretching modes (1579, 1460, and 1379 cm^{-1} modes in the neutral) by about 30 - 40 cm^{-1} is

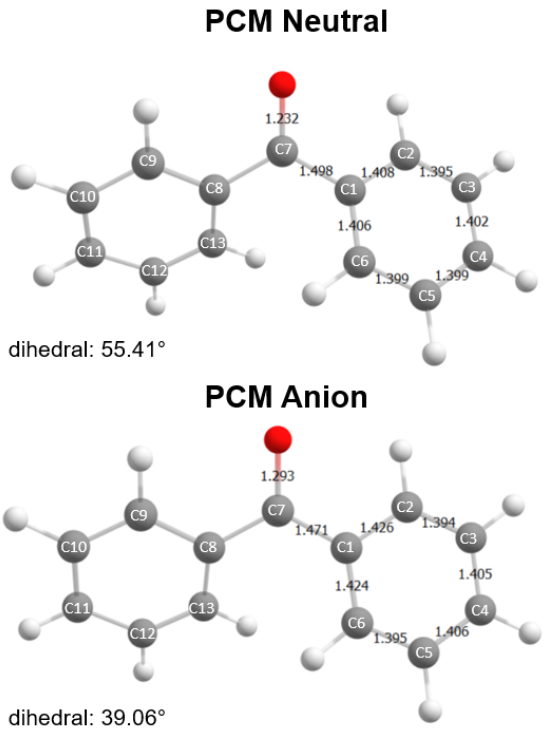

Figure 7: Theoretically predicted molecular geometry of neutral benzophenone and its corresponding radical anion in THF PCM model. A comparison of PCM structures with gas-phase structures can be found in the SI.

suggestive that, in solution, the electron density is added to an anti-bonding orbital changing the π bond order and, therefore, also the force constants relative to neutral naphthalene. Perhaps even more convincing evidence comes from the observation of high IR band intensities for Np^- assignable to large charge flux between naphthalene rings via motion along the bond alternation mode. We conclude that the calculations presented here for the anion are representative of the true solution phase where significant localization of the excess electron occurs into the π^* orbital on naphthalene.

The calculations also show aromatic ring framework distortions for Bp^- compared to Bp (Figure 7), but the largest effects arise around the carbonyl moiety where much of the excess charge in Bp^- is predicted to reside. This change in bonding around the carbonyl upon the addition of an electron to neutral Bp (a longer C-O bond and shorter C1-C7(C8) bonds) is accompanied by a significant change in the twist between the two phenyls.

The Bp structure exhibits a dihedral angle between the two rings of 54 °in the gas phase with a similar value of 55 °in a dielectric matching THF. Note that these values align closely with the dihedral angle of approximately 56 °obtained from X-ray crystallography of crystalline Bp, as observed experimentally.[92] In contrast, the optimized structure of the Bp^- displayed a significantly more planar conformation, with dihedral angles of 36 °in the gas phase and 39 °in liquid THF. This increased planarization of Bp is also in line with experimentally measured Raman spectra[88] that supported the shift to a more planar structure and the localization of the added electron density to the carbonyl functional moiety.

C. Progressive stabilization by solvent

There have been numerous experimental and theoretical studies in the past that investigated VEA shifts of the excess electron upon solvation pointing to increased stability of the radical anion in solution.[1,7,10] However, this is the first measurement of the impact of complete bulk solvation on the energetics. The addition of methanol (MeOH) ligands to $Bp^-(MeOH)_n$ in the gas phase has been shown to shift its $EA_{n=0} = 0.91$ eV, to $EA_{n=1} = 1.29$ eV, $EA_{n=2} = 1.65$ eV, $EA_{n=3} = 1.74$ eV.[74] In a recent paper, Verlet and coworkers observe that upon solvation of the anthracene anion by water, on average each of the first shell waters increases the VDE by ∼0.2 eV.[93] They also observe the singlet-triplet splitting, 1.93 eV, does not change on solvation. Similar stabilization takes place also for species unstable in the gas phase like $Np^-(Bz)_n$ or $Np^-(H_2O)_n$, which become stable by attaching a single ($n = 1$) ligand molecule evidenced by measured positive EA being $EA_{Np^-(Bz)_1} = 0.03$ eV[7] and $EA_{Np^-(H_2O)_1} = 0.11$ eV.[10]

Kostal et. al.[28] investigated step-by-step the whole solvation process from the isolated gas phase species all the way to the liquid bulk. It was shown there that the Bz^- requires between 7-10 ammonia molecules to reach negative VDEs for the excess electron, i.e., to stabilize the species. Also, it takes hundreds of solvent molecules to converge to the VDE bulk value. A related study of the same system in bulk liquid ammonia demonstrates that while the excess electron is well localized on the benzene moiety (leading also to its Jahn-Teller distortions) the electronic stability of Bz^- results dominantly from interactions with the solvent ammonia molecules providing dielectric stabilization.[27]

D. Mechanism of excess charge stabilization

From the above considerations we would argue that for both investigated molecules, it is the change in the dielectric constant from the presence of solvent that provides the main mechanism to stabilize the excess electron and this dominant effect is being well recovered by the PCM calculations. This conclusion is independently supported by applying the simple Born-Haber cycle model – see Table 2 and the detailed section in the SI for a quantitative comparison – which we envision to be operative in analogy to the recent study of sequential solvation Bz^- in ammonia.[28] The fact that the stabilization mechanism for radical anions is dominantly an electrostatic mean

field effect, implies two characteristic properties of aromatic radical anions in solution: firstly, the shape of the SOMO (as well as the lower-lying MOs) should remain largely unaffected by solvation. Secondly, the fact that a simple Born model appears to be well suited to describe all MO shifts for the radical anion according simply to the dielectric constant, opens up the possibility of exploring the tuning of the stability and reactivity of radical anions as reflected in the respective ADE values. ADE can, in turn, be estimated from the measured VDE peak positions and widths of the spectrally isolated SOMO band. Thus, within the range allowed by practical solvents, a liquid-jet PE measurement can verify VDE tuning solely considering characteristic dielectric constant. For example, the VDEs, and correspondingly the ADEs, could be tuned using, on the one hand, e.g., acetonitrile (ε_r = 37.5) and, on the other hand, for example, toluene (ε_r = 2.4). Binary mixtures of the two solvents can be produced at any ratio allowing to continuously adjust the dielectric constant as demonstrated in reference 94. Assuming solvent mixing is happening also at the nanoscale, the VDEs of Np^- could be tuned between -3.05 and -1.85 eV while those of Bp^- could be tuned between -3.83 and -2.80 eV. Acetonitrile may be a better-suited solvent to increase the stability of radical anion intermediate, but it also stabilizes a solvated electron.[95] Toluene on the other hand increases the reactivity, with that only moderate concentrations of radical anion species can be achieved in this non-polar solvent. Researchers on aromatic carbanion intermediates have long worked in a narrow range of ethereal solvents, and have found that the counter-cation provides the most subtle control on tuning the chemistry, as well as exploiting crown ethers to sequester alkali ions. Our measurements have not yet explored this tunability, but with the binding energy precision now possible using cut-off based calibration, we can anticipate that such information will be forthcoming. For the time being, we note that given prior literature suggests that Np^- exists in contact ion pairs with K^+, the VDE and ADEs reported here therefore most likely correspond to the energetics from the ion pair, rather than the free Np^-.

E. Reactivity in the context of Birch chemistry

The above considerations influence the chemical reaction dynamics which we now discuss in the context of Birch reduction, where electrons liberated from an alkali metal act as reducing agents. Mechanistically, Birch reduction proceeds in multiple steps involving sequential addition of electrons and protons (the latter typically provided by a suitable alcohol), eventually leading to selective hydrogenation of aromatic compounds – as Figure 8 illustrates the iconic example of the conversion of benzene into 1,4-cyclohexadiene.[2] The present study is particularly relevant for the first key step of this process, namely, the formation of the aromatic radical anions.

The classic Birch reduction is conducted in liquid ammonia[2] which brings in the following issues. First, ammonia is liquid only below -33°C which requires refrigeration of the reaction mixture. Second, liquid ammonia strongly stabilizes solvated electrons and dielectrons,[19] which is a competing process to the formation of aromatic radical anions. Indeed, in liquid ammonia at higher electron concentrations it is more favorable to form solvated di-electrons than benzene radical anions.[46] The choice of other polar media such as THF or acetonitrile for example leads to less stabilization of the solvated electrons which persist only on micro- to millisecond timescales.[13,95] At the same time, aromatic radical anions can be formed in these solutions at up to molar concentrations. Concerning the first step of Birch reduction, one is seeking a solvent providing the best compromise between stability and reactivity of the aromatic radical anions.

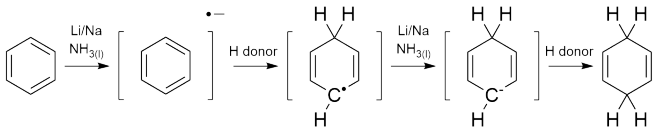

Figure 8: Schematic depiction of the two main reaction steps of the Birch reduction of benzene in liquid ammonia.

Recent studies explored various solvent environments with the aim of realizing Birch reduction at room temperature.[5] An important conclusion was that Birch reaction could be achieved by using binary solutions but that for good overall yield, an amine co-solvent must be present. For example, in a mixture of THF and ethylenediamine comparable substituted benzene hydrogenation yields are achieved as for the reaction carried out in liquid ammonia, while for a pure THF solution, no Birch reduction is observed.[5] Most likely, the limiting step that prevents the hydrogenation reaction in THF is the protonation of the formed aromatic radical anion as the second step of the Birch reduction process (Figure 8). A choice of simultaneously optimizing the solvent, alkali metal, and suitable proton donor, thus remains the task for future studies going beyond investigating the formation of the aromatic radical anion as the first step of the Birch reduction process.

5. CONCLUSION

We have conducted the first quantitative study of binding energies of the valence electrons of aromatic radical anions in the solution phase employing a combination of LJ-PES measurements and quantum chemical calculations.

First, we characterized the pure THF solvent by LJ-PES measurements in conjunction with AIMD simulations and G_0W_0 calculations. Notably, all PE peaks shift to lower binding energy by practically the same value, *ca.*

1.28 eV and this gas-liquid solvation shift can be rationalized in terms of the Born solvation model.

Next, we investigated the electronic structure of Np/Np$^-$ and of Bp/Bp$^-$ in THF. We determined accurately the corresponding VDEs employing recently developed calibration protocols.[24–26] Wherever feasible, the assignment of the measured PE features of the radical anion is established by reference to known energetics of the solution-phase electronic state energies of the Np and Bp neutrals. For greater insight, we performed electronic structure calculations to understand the molecular orbital parentage for each peak as well as to test the ability of theory to reproduce the measured VIEs and VDEs.

By analyzing the electronic structure differences between the neutral species and their anionic counterparts, we gained valuable insights into the influence of the excess electron on the studied molecular structures. The calculations also facilitated an accurate estimation of the large gas-liquid shift in electron BEs for the radical anions (2.3 - 2.7 eV) and enabled us to determine the delocalization patterns of the excess electron. For example, the excess electron is bound in a qualitatively different manner to the two radical anions confirming previous assignments: while the electron is delocalized over the entire ring system in Np$^-$, much of the SOMO density for Bp$^-$ lies on the bridging carbonyl. If the density were entirely localized on the carbonyl we would expect a larger gas-liquid shift than for Np$^-$. Instead, our calculations suggest a similar or smaller solvation shift (with the computed gas-liquid shift in good agreement with experiment) suggesting that closing of the torsion angle between the two benzene planes allows the excess electron charge density to be more spread out into the π system of the two phenyl rings, as it is in the gas phase.

These outcomes provide a crucial understanding of the stabilization mechanism of radical anion species upon solvation which turns out to be dominantly an electrostatic mean field effect. Thus, the change of the dielectric continuum – defined by the dielectric constant of the solvent environment – determines the eBE increase which leads to the stabilization of the excess electron of Np$^-$ and Bp$^-$. In this context, the formation of Np$^-$ in the solution can be rationalized employing our previous computational studies on the stabilization of Bz$^-$ upon solvation in liquid ammonia.[27,28]

Third, we find very good agreement of the reductive potentials extracted from the present LJ-PES measurements of Np$^-$ and Bp$^-$ in THF with electrochemical data employing the ferrocene standard with literature values from CV measurements.[1] This allowed us to relate directly to the chemical reactivity of these radical anions in solution to the findings of solvent-induced shifts being solely determined by the dielectric constant of the solvent itself. Finally, we discuss how we can move toward more directly quantifying different microscopic environments and their energetic impact on the carbanion intermediates so as to screen for suitable media for the Birch process that move beyond the practical difficulties associated with liquid ammonia conditions.

SUPPORTING INFORMATION

ACKNOWLEDGEMENT

T.N. acknowledges support from University of Chemistry and Technology Prague where she is enrolled as PhD. students and from the IMPRS for Many Particle Systems in Structured Environments. B.M.Y. and S.E.B. acknowledge funding and supplementary support for travel to Berlin from the US National Science Foundation (CHE-1665532). P.J. acknowledges support from the European Research Council via an ERC Advanced Grant no. 101095957.

REFERENCES

[1] N. G. Connelly and W. E. Geiger, "Chemical redox agents for organometallic chemistry," Chemical Reviews **96**, 877–910 (1996).
[2] A. J. Birch, "117. reduction by dissolving metals. part i," J. Chem. Soc. , 430–436 (1944).
[3] D. K. Joshi, J. W. Sutton, S. Carver, and J. P. Blanchard, "Experiences with commercial production scale operation of dissolving metal reduction using lithium metal and liquid ammonia," Organic Process Research & Development **9**, 997–1002 (2005).
[4] A. J. Birch, "The birch reduction in organic synthesis," Pure and Applied Chemistry **68**, 553–556 (1996).
[5] J. Burrows, S. Kamo, and K. Koide, "Scalable birch reduction with lithium and ethylenediamine in tetrahydrofuran," Science **374**, 741–746 (2021).
[6] J. A. Linthorst, "An overview: origins and development of green chemistry," Foundations of Chemistry **12**, 1572–8463 (2010).
[7] J. K. Song, N. K. Lee, S. Y. Han, and S. K. Kim, "The naphthalene-benzene anion: Anion complex of aromatic hydrocarbons with the smallest electron affinity," The Journal of Chemical Physics **117**, 9973–9976 (2002).
[8] J. Zhao, W. Wu, J. Sun, and S. Guo, "Triplet photosensitizers: from molecular design to applications," Chem. Soc. Rev. **42**, 5323–5351 (2013).
[9] M. Suto, X. Wang, J. Shan, and L. Lee, "Quantitative photoabsorption and fluorescence spectroscopy of benzene, naphthalene, and some derivatives at 106–295 nm," Journal of Quantitative Spectroscopy and Radiative Transfer **48**, 79–89 (1992).
[10] S. A. Lyapustina, S. Xu, J. M. Nilles, and K. H. Bowen Jr, "Solvent-induced stabilization of the naphthalene anion by water molecules: A negative cluster ion photoelectron spectroscopic study," The Journal of Chemical Physics **112**, 6643–6648 (2000).
[11] H. E. Zimmerman, "A mechanistic analysis of the birch reduction," Accounts of Chemical Research **45**, 164–170 (2012).
[12] N. Greenwood and A. Earnshaw, *Chemistry of the Elements*, second edition ed. (Butterworth-Heinemann, Oxford, 1997).
[13] R. A. Marasas, T. Iyoda, and J. R. Miller, "Benzene radical ion in equilibrium with solvated electrons," The Journal of Physical Chemistry A **107**, 2033–2038 (2003).
[14] M. Faubel, S. Schlemmer, and J. P. Toennies, "A molecular beam study of the evaporation of water from a liquid jet," Zeitschrift für Physik D Atoms, Molecules and Clusters **10** (1988).
[15] M. Faubel, B. Steiner, and J. P. Toennies, "Photoelectron spectroscopy of liquid water, some alcohols, and pure nonane in free micro jets," The Journal of Chemical Physics **106**, 9013–9031 (1997).

[16]B. Winter and M. Faubel, "Photoemission from liquid aqueous solutions," Chemical Reviews **106**, 1176–1211 (2006).

[17]J. B. Kim, C. Schoenwaelder, and S. H. Glenzer, "Development and characterization of liquid argon and methane microjets for high-rep-rate laser-plasma experiments," Review of Scientific Instruments **89**, 10K105 (2018).

[18]T. Buttersack, P. E. Mason, P. Jungwirth, H. C. Schewe, B. Winter, R. Seidel, R. S. McMullen, and S. E. Bradforth, "Deeply cooled and temperature controlled microjets: Liquid ammonia solutions released into vacuum for analysis by photoelectron spectroscopy," Review of Scientific Instruments **91**, 043101 (2020).

[19]T. Buttersack, P. E. Mason, R. S. McMullen, H. C. Schewe, T. Martinek, K. Brezina, M. Crhan, A. Gomez, D. Hein, G. Wartner, R. Seidel, H. Ali, S. Thürmer, O. Marsalek, B. Winter, S. E. Bradforth, and P. Jungwirth, "Photoelectron spectra of alkali metal-ammonia microjets: From blue electrolyte to bronze metal," Science **368**, 1086–1091 (2020).

[20]R. Seidel, B. Winter, and S. E. Bradforth, "Valence electronic structure of aqueous solutions: Insights from photoelectron spectroscopy," Annual Review of Physical Chemistry **67**, 283–305 (2016).

[21]D. Nolting, N. Ottosson, M. Faubel, I. V. Hertel, and B. Winter, "Pseudoequivalent nitrogen atoms in aqueous imidazole distinguished by chemical shifts in photoelectron spectroscopy," Journal of the American Chemical Society **130**, 8150–8151 (2008).

[22]T. Lewis, B. Winter, A. C. Stern, M. D. Baer, C. J. Mundy, D. J. Tobias, and J. C. Hemminger, "Dissociation of strong acid revisited: X-ray photoelectron spectroscopy and molecular dynamics simulations of hno3 in water," The Journal of Physical Chemistry B **115**, 9445–9451 (2011).

[23]A. Szabo and N. S. Ostlund, *Modern quantum chemistry: introduction to advanced electronic structure theory* (Courier Corporation, 2012).

[24]S. Thuermer, S. Malerz, F. Trinter, U. Hergenhahn, C. Lee, D. Neumark, G. Meijer, B. Winter, and I. Wilkinson, "Accurate vertical ionization energy and work function determinations of liquid water and aqueous solutions," Chemical Science **12**, 10558–10582 (2021).

[25]L. Pérez Ramírez, A. Boucly, F. Saudrais, F. Bournel, J.-J. Gallet, E. Maisonhaute, A. R. Milosavljević, C. Nicolas, and F. Rochet, "The fermi level as an energy reference in liquid jet x-ray photoelectron spectroscopy studies of aqueous solutions," Phys. Chem. Chem. Phys. **23**, 16224–16233 (2021).

[26]H. C. Schewe, K. Brezina, V. Kostal, P. E. Mason, T. Buttersack, D. M. Stemer, R. Seidel, W. Quevedo, F. Trinter, B. Winter, *et al.*, "Photoelectron spectroscopy of benzene in the liquid phase and dissolved in liquid ammonia," The Journal of Physical Chemistry B **126**, 229–238 (2021).

[27]K. Brezina, P. Jungwirth, and O. Marsalek, "Benzene radical anion in the context of the birch reduction: When solvation is the key," The Journal of Physical Chemistry Letters **11**, 6032–6038 (2020).

[28]V. Kostal, K. Brezina, O. Marsalek, and P. Jungwirth, "Benzene radical anion microsolvated in ammonia clusters: Modeling the transition from an unbound resonance to a bound species," The Journal of Physical Chemistry A **125**, 5811–5818 (2021).

[29]R. Follath, J. S. Schmidt, F. Siewert, K. Holldack, W. Zeschke, T.and Frentrup, D. Schmitz, and K. J. S. Sawhney, "Commissioning of the u49/2-pgm1 beamline," AIP Conf. Proc. **705** (2003).

[30]R. Seidel, M. N. Pohl, H. Ali, B. Winter, and E. F. Aziz, "Advances in liquid phase soft-x-ray photoemission spectroscopy: A new experimental setup at BESSY II," Review of Scientific Instruments **88** (2017).

[31]S. Malerz, H. Haak, F. Trinter, A. B. Stephansen, C. Kolbeck, M. Pohl, U. Hergenhahn, G. Meijer, and B. Winter, "A setup for studies of photoelectron circular dichroism from chiral molecules in aqueous solution," Review of Scientific Instruments **93**, 015101 (2022).

[32]B. Winter, S. Thürmer, and I. Wilkinson, "Absolute electronic energetics and quantitative work functions of liquids from photoelectron spectroscopy," Accounts of Chemical Research **56**, 77–85 (2023).

[33]J. Hutter, M. Iannuzzi, F. Schiffmann, and J. VandeVondele, "cp2k: atomistic simulations of condensed matter systems," Wiley Interdisciplinary Reviews: Computational Molecular Science **4**, 15–25 (2014).

[34]J. VandeVondele, M. Krack, F. Mohamed, M. Parrinello, T. Chassaing, and J. Hutter, "Quickstep: Fast and accurate density functional calculations using a mixed gaussian and plane waves approach," Computer Physics Communications **167**, 103–128 (2005).

[35]T. D. Kühne, M. Iannuzzi, M. Del Ben, V. V. Rybkin, P. Seewald, F. Stein, T. Laino, R. Z. Khaliullin, O. Schütt, F. Schiffmann, *et al.*, "Cp2k: An electronic structure and molecular dynamics software package-quickstep: Efficient and accurate electronic structure calculations," The Journal of Chemical Physics **152** (2020).

[36]J. P. Perdew, K. Burke, and M. Ernzerhof, "Generalized gradient approximation made simple," Physical review letters **77**, 3865 (1996).

[37]Y. Zhang and W. Yang, "Comment on "generalized gradient approximation made simple"," Physical Review Letters **80**, 890 (1998).

[38]C. Adamo and V. Barone, "Toward reliable density functional methods without adjustable parameters: The pbe0 model," The Journal of chemical physics **110**, 6158–6170 (1999).

[39]L. Goerigk and S. Grimme, "A thorough benchmark of density functional methods for general main group thermochemistry, kinetics, and noncovalent interactions," Physical Chemistry Chemical Physics **13**, 6670–6688 (2011).

[40]S. Goedecker, M. Teter, and J. Hutter, "Separable dual-space gaussian pseudopotentials," Physical Review B **54**, 1703 (1996).

[41]M. Guidon, J. Hutter, and J. VandeVondele, "Auxiliary density matrix methods for hartree- fock exchange calculations," Journal of chemical theory and computation **6**, 2348–2364 (2010).

[42]G. Bussi, D. Donadio, and M. Parrinello, "Canonical sampling through velocity rescaling," The Journal of chemical physics **126** (2007).

[43]J. Wilhelm, M. Del Ben, and J. Hutter, "Gw in the gaussian and plane waves scheme with application to linear acenes," Journal of Chemical Theory and Computation **12**, 3623–3635 (2016).

[44]E. Pluharova, P. Slavicek, and P. Jungwirth, "Modeling photoionization of aqueous dna and its components," Accounts of Chemical Research **48**, 1209–1217 (2015).

[45]K. Brezina, V. Kostal, P. Jungwirth, and O. Marsalek, "Electronic structure of the solvated benzene radical anion," The Journal of Chemical Physics **156**, 014501 (2022).

[46]T. Nemirovich, V. Kostal, J. Copko, H. C. Schewe, S. Bohacova, T. Martinek, T. Slanina, and P. Jungwirth, "Bridging electrochemistry and photoelectron spectroscopy in the context of birch reduction: Detachment energies and redox potentials of electron, dielectron, and benzene radical anion in liquid ammonia," Journal of the American Chemical Society **144**, 22093–22100 (2022).

[47]B. O. Roos, "Multiconfigurational quantum chemistry," in *Theory and Applications of Computational Chemistry* (Elsevier, 2005) Chap. 25, pp. 725–764.

[48]F. Neese, "The orca program system," Wiley Interdisciplinary Reviews: Computational Molecular Science **2**, 73–78 (2012).

[49]F. Neese, "Software update: The orca program system—version 5.0," Wiley Interdisciplinary Reviews: Computational Molecular Science **12**, e1606 (2022).

[50]E. Cances, B. Mennucci, and J. Tomasi, "A new integral equation formalism for the polarizable continuum model: Theoretical background and applications to isotropic and anisotropic dielectrics," The Journal of chemical physics **107**, 3032–3041 (1997).

[51]J. Tomasi, B. Mennucci, and E. Cancès, "The ief version of the pcm solvation method: an overview of a new method addressed to study molecular solutes at the qm ab initio level," Journal of Molecular Structure: THEOCHEM **464**, 211–226 (1999).

[52] J. Tomasi, B. Mennucci, and R. Cammi, "Quantum mechanical continuum solvation models," Chemical reviews **105**, 2999–3094 (2005).

[53] M. Cossi and V. Barone, "Solvent effect on vertical electronic transitions by the polarizable continuum model," The Journal of Chemical Physics **112**, 2427–2435 (2000).

[54] M. Cossi and V. Barone, "Separation between fast and slow polarizations in continuum solvation models," The Journal of Physical Chemistry A **104**, 10614–10622 (2000).

[55] A. D. Becke, "A new mixing of hartree–fock and local density-functional theories," The Journal of chemical physics **98**, 1372–1377 (1993).

[56] S. Grimme, S. Ehrlich, and L. Goerigk, "Effect of the damping function in dispersion corrected density functional theory," Journal of Computational Chemistry **32**, 1456–1465 (2011).

[57] S. Grimme, J. Antony, S. Ehrlich, and H. Krieg, "A consistent and accurate ab initio parametrization of density functional dispersion correction (dft-d) for the 94 elements h-pu," The Journal of chemical physics **132**, 154104 (2010).

[58] R. A. Kendall, T. H. Dunning Jr, and R. J. Harrison, "Electron affinities of the first-row atoms revisited. systematic basis sets and wave functions," The Journal of chemical physics **96**, 6796–6806 (1992).

[59] C. Angeli, R. Cimiraglia, S. Evangelisti, T. Leininger, and J.-P. Malrieu, "Introduction of n-electron valence states for multireference perturbation theory," The Journal of Chemical Physics **114**, 10252–10264 (2001).

[60] C. Angeli, R. Cimiraglia, and J.-P. Malrieu, "N-electron valence state perturbation theory: a fast implementation of the strongly contracted variant," Chemical physics letters **350**, 297–305 (2001).

[61] C. Angeli, R. Cimiraglia, and J.-P. Malrieu, "n-electron valence state perturbation theory: A spinless formulation and an efficient implementation of the strongly contracted and of the partially contracted variants," The Journal of chemical physics **117**, 9138–9153 (2002).

[62] J. H. D. Eland, *Photoelectron spectroscopy: an introduction to ultraviolet photoelectron spectroscopy in the gas phase* (Elsevier, 2013).

[63] L. Goerigk and S. Grimme, "Efficient and accurate double-hybrid-meta-gga density functionals-evaluation with the extended gmtkn30 database for general main group thermochemistry, kinetics, and noncovalent interactions," Journal of chemical theory and computation **7**, 291–309 (2011).

[64] M. J. Frisch, G. W. Trucks, H. B. Schlegel, G. E. Scuseria, M. A. Robb, J. R. Cheeseman, G. Scalmani, V. Barone, G. A. Petersson, H. Nakatsuji, X. Li, M. Caricato, A. V. Marenich, J. Bloino, B. G. Janesko, R. Gomperts, B. Mennucci, H. P. Hratchian, J. V. Ortiz, A. F. Izmaylov, J. L. Sonnenberg, D. Williams-Young, F. Ding, F. Lipparini, F. Egidi, J. Goings, B. Peng, A. Petrone, T. Henderson, D. Ranasinghe, V. G. Zakrzewski, J. Gao, N. Rega, G. Zheng, W. Liang, M. Hada, M. Ehara, K. Toyota, R. Fukuda, J. Hasegawa, M. Ishida, T. Nakajima, Y. Honda, O. Kitao, H. Nakai, T. Vreven, K. Throssell, J. A. Montgomery, Jr., J. E. Peralta, F. Ogliaro, M. J. Bearpark, J. J. Heyd, E. N. Brothers, K. N. Kudin, V. N. Staroverov, T. A. Keith, R. Kobayashi, J. Normand, K. Raghavachari, A. P. Rendell, J. C. Burant, S. S. Iyengar, J. Tomasi, M. Cossi, J. M. Millam, M. Klene, C. Adamo, R. Cammi, J. W. Ochterski, R. L. Martin, K. Morokuma, O. Farkas, J. B. Foresman, and D. J. Fox, "Gaussian 16 Revision A.03," (2016), gaussian Inc. Wallingford CT.

[65] M. Dampc, B. Mielewska, M. R. Siggel-King, G. C. King, and M. Zubek, "Threshold photoelectron spectra of tetrahydrofuran over the energy range 9–29 ev," Chemical Physics **359**, 77–81 (2009).

[66] A. Giuliani, P. Limão-Vieira, D. Duflot, A. R. Milosavljevic, B. P. Marinkovic, S. V. Hoffmann, N. Mason, J. Delwiche, and M.-J. Hubin-Franskin, "Electronic states of neutral and ionized tetrahydrofuran studied by vuv spectroscopy and ab initio calculations," The European Physical Journal D **51**, 97–108 (2009).

[67] Z. Baird, P. Uusi-Kyyny, J. Pokki, and et al., "Vapor pressures, densities, and pc-saft parameters for 11 bio-compounds," Int. J. Thermophysics **40** (2019), 10.1007/s10765-019-2570-9.

[68] D. T. Bowron, J. L. Finney, and A. K. Soper, "The structure of liquid tetrahydrofuran," Journal of the American Chemical Society **128**, 5119–5126 (2006).

[69] H. Grosch, Z. Sárossy, H. Egsgaard, and A. Fateev, "Uv absorption cross-sections of phenol and naphthalene at temperatures up to 500°c," Journal of Quantitative Spectroscopy and Radiative Transfer **156**, 17–23 (2015).

[70] J. B. Birks, *Photophysics of aromatic molecules* (Wiley, 1970).

[71] M. Montalti, A. Credi, L. Prodi, and M. T. Gandolfi, *Handbook of photochemistry* (CRC press, 2006).

[72] J. Segarra-Martí, E. Zvereva, M. Marazzi, J. Brazard, E. Dumont, X. Assfeld, S. Haacke, M. Garavelli, A. Monari, J. Léonard, and I. Rivalta, "Resolving the singlet excited state manifold of benzophenone by first-principles simulations and ultrafast spectroscopy," Journal of Chemical Theory and Computation **14**, 2570–2585 (2018).

[73] M. C. Cockett, H. Ozeki, K. Okuyama, and K. Kimura, "Vibronic coupling in the ground cationic state of naphthalene: a laser threshold photoelectron [zero kinetic energy (zeke)-photoelectron] spectroscopic study," The Journal of chemical physics **98**, 7763–7772 (1993).

[74] I. Yagi, T. Maeyama, A. Fujii, and N. Mikami, "Stepwise solvatochromism of ketyl anions in the gas phase: Photodetachment excitation spectroscopy of benzophenone and acetophenone radical anions microsolvated with methanol," The Journal of Physical Chemistry A **111**, 7646–7652 (2007).

[75] E. McAlduff and D. Bunbury, "Photoelectron spectra of some aromatic mono-and di-ketones," Journal of Electron Spectroscopy and Related Phenomena **17**, 81–89 (1979).

[76] A. Roy, R. Seidel, G. Kumar, and S. E. Bradforth, "Exploring redox properties of aromatic amino acids in water: Contrasting single photon vs resonant multiphoton ionization in aqueous solutions," The Journal of Physical Chemistry B **122**, 3723–3733 (2018).

[77] K. D. Jordan and P. D. Burrow, "Studies of the temporary anion states of unsaturated hydrocarbons by electron transmission spectroscopy," Accounts of Chemical Research **11**, 341–348 (1978).

[78] J. Schiedt and R. Weinkauf, "Photodetachment photoelectron spectroscopy of mass selected anions: anthracene and the anthracene-h2o cluster," Chemical Physics Letters **266**, 201–205 (1997).

[79] M. J. Bedard-Hearn, R. E. Larsen, and B. J. Schwartz, "The role of solvent structure in the absorption spectrum of solvated electrons: Mixed quantum/classical simulations in tetrahydrofuran," The Journal of Chemical Physics **122**, 134506 (2005).

[80] A. E. Bragg and B. J. Schwartz, "The ultrafast charge-transfer-to-solvent dynamics of iodide in tetrahydrofuran. 1. exploring the roles of solvent and solute electronic structure in condensed-phase charge-transfer reactions," The Journal of Physical Chemistry B **112**, 483–494 (2008).

[81] I. A. Shkrob, "Ammoniated electron as a solvent stabilized multimer radical anion," The Journal of Physical Chemistry A **110**, 3967–3976 (2006).

[82] F. Uhlig, O. Marsalek, and P. Jungwirth, "Unraveling the complex nature of the hydrated electron," The Journal of Physical Chemistry Letters **3**, 3071–3075 (2012).

[83] L. Kevan, "Solvated electron structure in glassy matrixes," Accounts of Chemical Research **14**, 138–145 (1981).

[84] G. S. Jas and K. Kuczera, "Ab initio calculations of s1 excited state vibrational spectra of benzene, naphthalene and anthracene," Chemical Physics **214**, 229–241 (1997).

[85] S. M. Beck, D. E. Powers, J. B. Hopkins, and R. E. Smalley, "Jet-cooled naphthalene. I. Absorption spectra and line profiles," The Journal of Chemical Physics **73**, 2019–2028 (2008).

[86] D. P. Craig, J. M. Hollas, M. F. Redies, S. C. Wait, Jr, and C. K. Ingold, "Analysis of the naphthalene vapour absorption bands at

3200Å. i. naphthalene h-8," Philosophical Transactions of the Royal Society of London. Series A, Mathematical and Physical Sciences **253**, 543–568 (1961).

[87]S. J. Kregel, G. K. Thurston, and E. Garand, "Photoelectron spectroscopy of anthracene and fluoranthene radical anions," The Journal of Chemical Physics **148**, 234306 (2018).

[88]A. Juneau and M. Frenette, "Raman spectra of persistent radical anions from benzophenone, fluorenone, 2, 2'-bipyridyl, 4, 4'-di-tert-butyl-2, 2'-dipyridyl, and anthracene: Excellent agreement between dft and experiment for highly delocalized radical systems," The Journal of Physical Chemistry B **125**, 1595–1603 (2021).

[89]H. Torii, Y. Ueno, A. Sakamoto, and M. Tasumi, "Vibrational spectra and electron-vibration interactions of the naphthalene radical anion - experimental and theoretical study," Canadian Journal of Chemistry **82**, 951–963 (2004).

[90]J. M. L. Martin, J. El-Yazal, and J.-P. François, "Structure and vibrational spectrum of some polycyclic aromatic compounds studied by density functional theory. 1. naphthalene, azulene, phenanthrene, and anthracene," The Journal of Physical Chemistry **100**, 15358–15367 (1996).

[91]S. D. Christesen and C. S. Johnson Jr, "Resonance raman spectra of naphthalene and naphthalene-d8 anions in thf," Journal of Raman Spectroscopy **14**, 53–58 (1983).

[92]E. B. Fleischer, N. Sung, and S. Hawkinson, "Crystal structure of benzophenone," The Journal of Physical Chemistry **72**, 4311–4312 (1968).

[93]A. Lietard, G. Mensa-Bonsu, and J. R. R. Verlet, "The effect of solvation on electron capture revealed using anion two-dimensional photoelectron spectroscopy," Nature Chemistry **13**, 737–742 (2021).

[94]G. Ritzoulis, N. Papadopoulos, and D. Jannakoudakis, "Densities, viscosities, and dielectric constants of acetonitrile + toluene at 15, 25, and 35 .degree.c," Journal of Chemical & Engineering Data **31**, 146–148 (1986).

[95]D. C. Grills and S. V. Lymar, "Solvated electron in acetonitrile: Radiation yield, absorption spectrum, and equilibrium between cavity- and solvent-localized states," The Journal of Physical Chemistry B **126**, 262–269 (2022).